PHYSICAL REVIEW D **96,** 015019 (2017)

Scalar production in association with a Z boson at the LHC and ILC: The mixed Higgs-radion case of warped models

Andrei Angelescu,[1,*] Grégory Moreau,[1,†] and François Richard[2,‡]

[1]*Laboratoire de Physique Théorique, Bât. 210, CNRS, Univ. Paris Sud, Université Paris-Saclay, F-91405 Orsay Cedex, France*

[2]*Laboratoire de l'Accélérateur Linéaire, IN2P3/CNRS, Univ. Paris Sud, Université Paris-Saclay, B.P. 34 F-91898 Orsay Cedex, France*

(Received 11 April 2017; published 19 July 2017)

The radion scalar field might be the lightest new particle predicted by extradimensional extensions of the standard model. It could thus lead to the first signatures of new physics at the LHC collider. We perform a complete study of the radion production in association with the Z gauge boson in the custodially protected warped model with a brane-localized Higgs boson addressing the gauge hierarchy problem. Radion-Higgs mixing effects are present. Such a radion production receives possibly resonant contributions from the Kaluza-Klein excitations of the Z boson as well as the extra neutral gauge boson (Z'). All the exchange and mixing effects induced by those heavy bosons are taken into account in the radion coupling and rate calculations. The investigation of the considered radion production at the LHC allows us to be sensitive to some parts of the parameter space but only the ILC program at high luminosity would cover most of the theoretically allowed parameter space via the studied reaction. Complementary tests of the same theoretical parameters can be realized through the high accuracy measurements of the Higgs couplings at the ILC. The generic sensitivity limits on the rates discussed for the LHC and ILC potential reach can be applied to the searches for other (light) exotic scalar bosons.

DOI: 10.1103/PhysRevD.96.015019

I. INTRODUCTION

Since the discovery of the Higgs boson and the completion of the standard model (SM), the search for new particles at the Large Hadron Collider (LHC) has become more and more intense. Precise measurements of Higgs couplings are the natural complement of these direct searches given that Higgs couplings could be influenced by virtual exchanges and/or mixing effects of exotic particles. Interestingly, new scalar fields (S), arising in various SM extensions, could both be directly produced and mix with the Higgs boson. Such scalars can still be as light as a few tens of GeV given that for example the vanishing sensitivity of the LEP collider searches when the ZZS coupling (to the Z boson) reaches $\sim 1/10$ of the ZZh (Higgs) coupling. LHC searches for scalars also suffer from limited sensitivity to light scalars; for instance the powerful investigation performed in the diphoton decay channel becomes inefficient for masses below $\sim$60 GeV given the trigger limitations. The future e^+e^- International Linear Collider (ILC) and CLIC, which shall collect more than 100 times the LEP luminosities and reach the TeV scale, are expected to improve the low scalar mass searches.

From the theoretical point of view, the warped extradimension scenario proposed by L. Randall and R. Sundrum (RS) [1] with a Higgs boson localized at (or close to) the TeV brane, being dual to composite Higgs models [2], remains one of the most attractive extensions of the SM. In particular, this is due to its elegant solution of the gauge hierarchy problem and its simple geometrical explanations of the fermion mass hierarchies [3,4]—in the case of matter in the bulk. The RS paradigm—including the dual composite Higgs scenarios—constitutes an alternative to the supersymmetric SM extensions, of a completely different nature. Nevertheless, both these kinds of SM extensions predict the existence of new scalar particles that could lead to clear experimental signatures at colliders. In the case of warped models, a predicted scalar is the so-called radion, which corresponds to the dilaton field through the AdS/CFT correspondence.

The phenomenology at colliders of the RS scenario is guided by the indirect constraints on the masses of the various Kaluza-Klein (KK) excitations. Let us thus shortly review the constraints on such a scenario arising from the electroweak precision tests (EWPT). In the RS model with a custodial symmetry gauged in the bulk [5], the bounds from EWPT can be reduced down to gauge boson masses $m_{KK} \gtrsim 3$–5 TeV [6–8] for the first KK excitation of say the photon, in the case of a purely brane-localized Higgs boson.[1] In RS versions with a bulk Higgs field unprotected by a custodial symmetry, these bounds become $m_{KK} \gtrsim 7.5$ TeV for a Higgs profile

*andrei.angelescu@th.u-psud.fr
†gregory.moreau@th.u-psud.fr
‡richard@lal.in2p3.fr

[1]$\sim$3 TeV for a bulk Higgs boson localized towards the TeV brane [9].

still addressing the gauge hierarchy problem ($\beta = 0$) [9,10],[2] and, $m_{KK} \gtrsim 13.5$ TeV for the brane-Higgs limit ($\beta \to \infty$) [10].

In contrast, within custodially protected warped models, the lightest KK excitations of fermions (custodians) can reach masses as low as the TeV scale while satisfying the EWPT affected by their loop contributions to the oblique parameters S,T [12] or their direct (mixing) corrections to the Zbb vertex [6].

The radion scalar field, corresponding to the fluctuations of the metric along the extra dimension, has a typical mass around the EW energy scale [13], within the standard mechanism of radius stabilization based on a bulk scalar field [14]. The EWPT (via the S,T,U parameters) and LEP limits allow radion masses between ~10 GeV and the TeV scale, depending on the curvature-scalar Higgs mixing [for SM fields on the infrared (IR) brane] [15].

Given those mass bounds, the radion might be the lightest new particle and thus appear as the first signature of warped models at colliders—before KK fermion [16] or KK gauge boson [17] productions. The detection of the radion would constitute the discovery of a second scalar field, after the Higgs boson observation. This new boson should then be disentangled from other scalar particles predicted by supersymmetric models or other scenarios with extended Higgs sectors.

The radion is mainly produced at the LHC by gluon-gluon fusion (see, e.g., Ref. [18] for a recent paper) but some model dependence might affect this process as we discuss now. The LHC data [19,20] on the Higgs rates[3] lead to $m_{KK} \gtrsim 11$ TeV for a brane-Higgs boson[4] within a custodially protected RS model [21].[5] These constraints arise essentially because of the contributions of KK modes to the Higgs production reaction with the highest cross section: the loop-induced gluon-gluon fusion (ggF) mechanism (see, e.g., Ref. [22]). To reduce this limit on the KK scale m_{KK} down to the TeV scale (comparable with EWPT limits), and in turn reconcile the related gravity scale at the IR brane with the fine-tuning problem, one may expect some new physics effects (brane-localized kinetic terms, different fermion representations under the custodial symmetry, cancellation mechanisms, etc.) in the triangular loop of the ggF mechanism, suppressing the KK mode contributions. This introduces some unknown model dependence in the Higgs ggF mechanism that would also affect the similar ggF process of the radion scalar production.

In contrast, the Higgs (h) production in association with an EW gauge boson ($V \equiv Z$, W), followed by the Higgs decay into a pair of bottom quarks, induces—due to KK mixing [23]—a limit of $m_{KK} \gtrsim 2.25$ TeV (3.25 TeV) with $y^* = 1.5$ ($y^* = 3$) for a brane-Higgs boson (and slightly above for a narrow bulk Higgs boson) still in custodial warped models [21]. Such values are acceptable from the fine-tuning point of view. Hence there is no strong reason to assume that this tree-level hV production is sensitive to unknown effects. A similar conclusion then holds for the radion (ϕ) production in association with a gauge boson V.

The ϕZ production in particular possesses other interests in some regions of the RS parameter space. For example, the radion discovery at the LHC through its ggF production is challenging if the radion mass satisfies $m_\phi < 2m_Z$, closing kinematically the golden channel $\phi \to ZZ$,[6] and is too small to allow for the detection of the diphoton decay $\phi \to \gamma\gamma$. The ϕZ production would then offer an additional on-shell Z boson that helps for the tagging of the final state. Another situation motivating the ϕZ production search is a suppression of the ggF rate due to a significant decrease of the radion coupling to gluons as occurs in some parameter regions.[7]

Regarding the future e^+e^- ILC machine, the ϕZ production would be the dominant radion production mode [24], similarly to the Higgs boson case. The ϕZ production in a leptonic machine is also an important channel because, as for the hZ channel, it allows for a decay independent search—based on the simple $2 \to 2$ body kinematics—that should permit, in particular, covering low radion masses that are challenging at the LHC.

Therefore, in this paper, we study the ϕZ production in custodially protected warped models with a brane-localized Higgs boson. The analytical calculations of the radion couplings allow us to compute the complete ϕZ production cross section, both at the LHC and ILC colliders. The LHC and ILC turn out to constitute complementary machines in regard to the ϕZ investigation. The ϕZ reaction proceeds through the s-channel exchange of the EW Z boson, its KK excitations as well as the extra Z' gauge boson (issued from the extended bulk custodial symmetry). All these contributions together with their interferences are taken into account. The effects of the various KK mixings in the radion couplings and KK exchanges in the s-channel are discussed, as well as the possibility to reconstruct the invariant mass of the first two resonant heavy boson eigenstates (mainly KK modes) almost degenerate in mass. Such a spectacular resonance observation would constitute a double discovery of the radion and first KK gauge bosons.

[2] ~2 TeV [9] with a deformed metric, with deviations from AdS geometry near the IR brane [11].

[3] These data constrain the Higgs-radion mixing to be small enough to recover a SM-like Higgs boson.

[4] ~7.25 TeV for a narrow bulk Higgs boson.

[5] Those limits hold for a maximal absolute value $y^* = 1.5$ of the anarchic dimensionless five-dimensional Yukawa coupling constants, and are even more severe for a larger value $y^* = 3$.

[6] Below this threshold, the channel $\phi \to ZZ^*$, into a virtual Z boson, may still allow us to reconstruct one on-shell Z boson decaying to charged lepton pairs.

[7] $m_\phi \gtrsim 200$ GeV and $\xi = \mathcal{O}(1)$, as shown in Ref. [18] (where the effect of the colored KK fermions on the ϕgg loop is neglected).

The resonant KK gauge boson detection through its decay to hZ is also quantitatively studied. Indeed, the ϕZ and hZ productions should be consistently analyzed together due to the $\phi - h$ mixing. In view of the obtained ϕZ and hZ rates, we discuss the possibilities of experimental observations that rely on favored radion decays, depending on the parameter space and, in particular, on m_ϕ values.

Furthermore, we propose in the present work a more general experimental technique to search for an inclusive final state $Z + X$ (where X represents any SM or new particles), followed by the decay $Z \to 2$ charged leptons, based on a cut on the distribution of the Z boson transverse momentum. The choice of the decay $Z \to \mu^+\mu^-$ is a tagging device to allow trigger and detection. Such a technique could also be applied for $X \equiv \phi$ in RS versions different from the present one, e.g., with lower resonant KK Z masses and/or favored gluon decays for the radion (so that the associated tagged Z becomes crucial for the detection). See for instance Ref. [25] for a recent warped model of this kind.

At this stage we also mention the related work on the search of the radion at colliders [18] as well as the more general literature on the radion phenomenology in warped scenarios with SM fields at the TeV brane [26], with only the Higgs boson stuck on the IR brane [27] or the whole SM field content propagating in the bulk [28]. Besides, there exists a connected study on the hZ production through resonant neutral KK gauge bosons [29].

The paper is organized as follows. In Sec. II, we present all the radion and Higgs couplings and calculate the KK mixing effects—applying the so-called mixed KK decomposition to the gauge boson sector. Then we provide the analytical and numerical results for the ϕZ and hZ (Sec. III) production cross sections at the LHC and ILC. The behaviors of these rates along the theoretical parameter space are explained there. In Sec. IV, experimental methods are proposed to detect the radion and/or (extra) KK gauge bosons. We conclude in the last section.

II. RADION AND HIGGS COUPLINGS

A. Model description

Our model is the RS scenario with the Higgs doublet localized on the IR brane, while the remaining fermionic and gauge fields are propagating in the bulk. The SM fermion mass hierarchy is generated through their wave function overlaps with the Higgs boson, as usually in this framework.

In the $(+----)$ convention that is used throughout this work, the well-known RS metric reads

$$ds^2 = e^{-2ky}\eta_{\mu\nu}dx^\mu dx^\nu - dy^2 \equiv g_{MN}dx^M dx^N, \qquad (1)$$

where uppercase roman letters refer to five-dimensional Lorentz indices and greek letters refer to four-dimensional indices, with k being the five-dimensional curvature scale, which is typically of the order of the Planck scale. The y coordinate, which parametrizes the position along the extra dimension, spans in the interval $[0, L]$. Throughout this work, we consider that kL, the so-called volume factor, is equal to 35, such that the hierarchy problem is addressed. For the time being, we denote by g_{MN} the *unperturbed* metric, and postpone the inclusion of the scalar fluctuations for Sec. II C.

We consider the custodial gauge symmetry implementation with a left-right parity [30] as well as a more general implementation allowing us potentially to address the $A_{\rm FB}^b$ [31] and $A_{\rm FB}^t$ [32] anomalies. These implementations predict the same gauge field content. The five-dimensional action containing the kinetic gauge terms reads

$$S_{\rm gauge}^{\rm 5D} = -\frac{1}{4}\int d^5x\sqrt{g}g^{AM}g^{BN}(\mathrm{tr}W_{AB}W_{MN} + \mathrm{tr}W'_{AB}W'_{MN} + B'_{AB}B'_{MN}), \qquad (2)$$

with W, W', and B' being the non-Abelian five-dimensional gauge field strengths associated to $\mathrm{SU}(2)_L$, $\mathrm{SU}(2)_R$, and $\mathrm{U}(1)_X$, respectively. We denote the corresponding five-dimensional gauge couplings as $g_L^{\rm 5D}$, $g_R^{\rm 5D}$, and $g_X^{\rm 5D}$, whose four-dimensional counterparts are given by $g_{L,R,X} \equiv g_{L,R,X}^{\rm 5D}/\sqrt{L}$. We did not include the gluon since it does not play a central role in our analysis. The mechanism responsible for the breaking of $\mathrm{SU}(2)_R \times \mathrm{SU}(2)_L \times \mathrm{U}(1)_X$ down to the EW symmetry group, $\mathrm{SU}(2)_L \times \mathrm{U}(1)_Y$, as well as the relations between the various couplings and mixing angles, are described in Ref. [5,30].

In the context of the extended gauge group mentioned in the previous paragraph, the brane-localized Higgs doublet gets promoted to a bidoublet of $\mathrm{SU}(2)_R \times \mathrm{SU}(2)_L$, uncharged under $\mathrm{U}(1)_X$. When it develops a vacuum expectation value (VEV), the Higgs bidoublet thus breaks, on the IR brane, together with the five-dimensional boundary conditions (BCs), the $\mathrm{SU}(2)_R \times \mathrm{SU}(2)_L \times \mathrm{U}(1)_X$ gauge group down to $\mathrm{U}(1)_{e.m.}$. times a global $\mathrm{SU}(2)_V$, the latter endowing the Higgs sector with a custodial symmetry, which keeps under control the contributions to the T parameter.

After the usual redefinition of the Higgs bidoublet, $H \to e^{kL}H$, the brane-localized action reads

$$S_{\rm Higgs}^{\rm 4D} = \int d^4x\left[\frac{1}{2}\eta^{\mu\nu}\mathrm{tr}D_\mu H^\dagger D_\nu H - \frac{\lambda_0}{4}(\mathrm{tr}H^\dagger H - v^2)^2\right]_{y=L}, \qquad (3)$$

where $v \simeq 246$ GeV (this is true, as it is shown in the next subsection, only in the limit where the KK partners decouple). Omitting the gluon, the covariant derivative is given, in terms of the five-dimensional gauge fields, by

$$D_\mu H = \partial_\mu H - i\sqrt{L}[g_L(W_\mu^a I_L^a)H + g_R H(W_\mu'^a I_R^a)^T], \quad (4)$$

with $I_{L,R}^a, a = 1, 2, 3$ being the $\mathrm{SU}(2)_{L,R}$ generators, proportional to the usual Pauli matrices. The $\sqrt{L}$ factor originates from using four-dimensional couplings instead of five-dimensional (dimensionful) couplings. Besides, due to the scalar bidoublet having null charge under $\mathrm{U}(1)_X$, the B' gauge field does not appear in the covariant derivative acting on H. After electroweak symmetry breaking, the Higgs bidoublet is parametrized as

$$H = \frac{v + h_0(x)}{\sqrt{2}} \begin{pmatrix} 0 & -1 \\ 1 & 0 \end{pmatrix}, \quad (5)$$

with h_0 being the (four-dimensional) Higgs field (before mixing with the radion). Putting all these ingredients together, the four-dimensional action has the following expression:

$$\begin{aligned} S_{\mathrm{Higgs}}^{\mathrm{4D}} = & \int \mathrm{d}^4 x L \left(1 + \frac{h_0}{v}\right)^2 \\ & \times \left[\bar{m}_W^2 (W_\mu - \alpha_W W_\mu')^2 + \frac{\bar{m}_Z^2}{2}(Z_\mu - \alpha_Z Z_\mu')^2\right]_{y=L} \\ & + \int \mathrm{d}^4 x \left[\frac{1}{2}(\partial_\mu h_0)^2 - \left(\frac{m_{h_0}^2}{2} h_0^2 + \frac{m_{h_0}^2}{2v} h_0^3 \right.\right. \\ & \left.\left. + \frac{m_{h_0}^2}{8v^2} h_0^4\right)\right]. \end{aligned} \quad (6)$$

Here, $V_\mu^2 \equiv \eta^{\mu\nu} V_\mu V_\nu$, and

$$\alpha_W = g_R/g_L, \qquad \alpha_Z = \sqrt{g_R^2/g_Z^2 - \sin^2\theta_W},$$
$$g_Z = g_L/\cos\theta_W,$$

θ_W being the weak mixing angle. From now on, unless otherwise stated, we consider the configuration $g_R = g_L$ (as enforced by a left-right parity [30]). The masses in the first line of Eq. (6) are given by $\bar{m}_{W,Z} = \frac{g_{L,Z} v}{2}$; as we show in the next section, they are not equal to the measured W and Z boson masses. Moreover, $m_{h_0}^2 = 2\lambda_0 v^2$ is the Higgs mass in the absence of mixing with the radion. The expression above is our starting point for deriving the (y-dependent) wave functions of the Z boson and its KK partners, as well as their couplings to the mixed Higgs-radion scalar fields.

B. KK gauge boson mixing

In this subsection, we outline the procedure employed for obtaining the masses and profiles of the Z boson and its KK partners. We denote the Z boson by Z_0, while its KK excitations (which here are also mass eigenstates) are referred to as Z_n, with $n = 1$ for the first KK level, $n = 2$ for the second one, and so on. Collecting several terms from Eqs. (2) and (6), the relevant part of the action reads, after EW symmetry breaking, as follows,

$$\begin{aligned} & S_{ZZ}^{\mathrm{5D}} \\ & = \int \mathrm{d}^5 x \sqrt{g}\left(-\frac{1}{4} g^{AB} g^{MN} Z_{AM} Z_{BN} - \frac{1}{4} g^{AB} g^{MN} Z'_{AM} Z'_{BN}\right) \\ & \quad + \int \mathrm{d}^5 x L \delta(y - L) \frac{\bar{m}_Z^2}{2} [Z_\mu(x,y) - \alpha_Z Z'_\mu(x,y)]^2, \end{aligned} \quad (7)$$

where $Z_{MN}^{(\prime)} \equiv \partial_M Z_N^{(\prime)} - \partial_N Z_M^{(\prime)}$. We choose to work in a gauge where the fifth component of the five-dimensional gauge fields, $Z_5^{(\prime)}$, is null.[8] Similarly to, e.g., Ref. [33], we perform a "mixed" KK decomposition, but applied to the gauge bosons,

$$\begin{aligned} Z_\mu(x,y) &= \frac{1}{\sqrt{L}} \sum_{n \geq 0} g_+^n(y) Z_{n,\mu}(x), \\ Z'_\mu(x,y) &= \frac{1}{\sqrt{L}} \sum_{n \geq 0} g_-^n(y) Z_{n,\mu}(x), \end{aligned} \quad (8)$$

where the (dimensionless) profiles $g_\pm^n$ obey the Neumann boundary condition at $y = L$ and the Neumann (+) or Dirichlet (−) boundary condition at $y = 0$. Choosing (−) boundary conditions at $y = 0$ for the Z' field eliminates its zero mode, thus reproducing the low-energy spectrum, made out of a single light Z boson (SM field content). Such a mixed decomposition allows us to include the boundary-localized mixing between the Z and Z' five-dimensional fields into the (coupled) equations of motion for g_+ and g_-, which in turn lead us to the exact expressions for the profiles and masses of the KK excitations of the Z boson.

By using the standard technique of varying the action in Eq. (7) with respect to the Z_μ and Z'_μ fields and then employing the KK decomposition in Eqs. (8), one gets the following equations of motions (EOM) for the profiles,

$$\begin{aligned} \partial_5(\mathrm{e}^{-2ky}\partial_5 g_+) + m^2 g_+ &= \bar{m}_Z^2 L \delta(y - L)[g_+(L) - \alpha_Z g_-(L)], \\ \partial_5(\mathrm{e}^{-2ky}\partial_5 g_-) + m^2 g_- &= -\alpha_Z \bar{m}_Z^2 L \delta(y - L)[g_+(L) \\ & \quad - \alpha_Z g_-(L)], \end{aligned} \quad (9)$$

with the BCs given by

$$g'_+(0) = g'_\pm(L) = g_-(0) = 0, \quad (10)$$

where the exponent "′" denotes differentiation with respect to y. For better readability, we have suppressed the n indices, which labeled the KK levels.

[8] While the 0 mode of the five-dimensional scalar field $Z_5^{(\prime)}$ is set to 0 by the BCs, one can interpret the KK modes of $Z_5^{(\prime)}$ as the longitudinal components of the KK Z bosons, $Z_{l\geq 1}^\mu$.

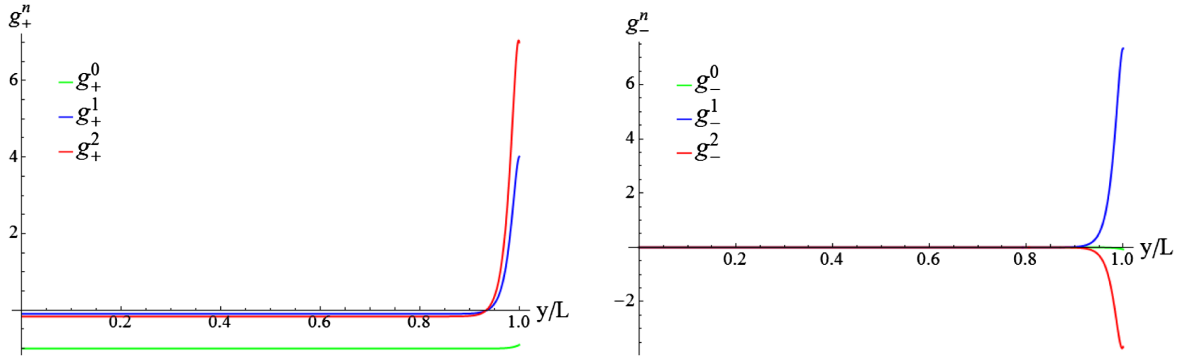

FIG. 1. Profiles of the Z_0 (green), Z_1 (blue), and Z_2 (red) fields, corresponding to (left) $(++)$ and (right) $(-+)$ boundary conditions, accordingly to Eq. (8). We have set $m_{KK} = 3$ TeV.

The presence of the delta functions in the EOM induces discontinuities in the first derivatives of the profiles at $y = L$. To find out by how much the derivatives "jump," we integrate the EOM in Eq. (9) from $L - \epsilon$ to L, and then take $\epsilon \to 0$, which gives us the following relations,

$$\begin{aligned} &\bar{m}_Z^2 L e^{-2kL}[g_+(L) - \alpha_Z g_-(L)] + g'_+(L_-) = 0, \\ &\alpha_Z \bar{m}_Z^2 L e^{-2kL}[g_+(L) - \alpha_Z g_-(L)] - g'_-(L_-) = 0, \end{aligned} \tag{11}$$

where we used the notation $\lim_{\epsilon \searrow 0} f(x - \epsilon) \equiv f(x_-)$. We now have all the prerequisites to calculate the profiles and the masses of the Z boson tower. Combining Eqs. (9)–(11), we find the well-known expressions for the profiles [3], which are expressed by the Bessel function of the first (J_α) and second (Y_α) kinds,

$$\begin{aligned} g_\pm^n = N_\pm^n e^{ky} &[J_{\frac{1}{2}\mp\frac{1}{2}}(x_n e^{-kL}) Y_1(x_n e^{k(y-L)}) \\ &- Y_{\frac{1}{2}\mp\frac{1}{2}}(x_n e^{-kL}) J_1(x_n e^{k(y-L)})], \end{aligned} \tag{12}$$

where $x_n \equiv 6 m_{Z_n}/m_{KK}$. The normalization constants $N_\pm^n$ are obtained by requiring that each Z_n field has a canonically normalized kinetic term, which translates to

$$\int_0^L \frac{dy}{L}(g_+^m g_+^n + g_-^m g_-^n) = \delta_{mn}. \tag{13}$$

We plot in Fig. 1 the $(++)$ and $(-+)$ profiles $g_\pm^n$ corresponding to the observed Z boson ($n = 0$) and to its two lightest KK modes ($n = 1, 2$). Notice that g_-^0 is slightly shifted from 0 close to L due to the $Z - Z'$ mixing. Also, g_+^0 is flat in most of the $[0, L]$ interval, with a small departure close to the IR brane, where the mixing of the SM-like Z boson with the heavier KK partners takes place. As for the lowest KK-Z profiles, i.e., $g_\pm^{1,2}$, they are all of comparable size and peaked towards $y = L$, signaling the usual KK partner localization close to the IR brane.

Meanwhile, the mass spectrum is obtained by solving the system of equations (11). One thus obtains

$$\begin{aligned} &\frac{6\bar{m}_Z^2 (kL)^2}{m_{KK}^2}[g_+(L) g'_-(L_-) - \alpha_Z^2 g'_+(L_-) g_-(L)] \\ &\quad + g'_+(L_-) g'_-(L_-) = 0. \end{aligned} \tag{14}$$

Notice that the normalization constants $N_\pm$ simplify in this equation. Since the lightest mode of the Z KK tower is identified with the observed Z boson, its mass should be equal to the measured $m_Z \simeq 91.2$ GeV. Imposing this condition determines the value of $\bar{m}_Z$ (and thus, as discussed later, of v) as a function of the mass of the first KK excitation of the photon/gluon, m_{KK}. In turn, knowing $\bar{m}_Z$, one can compute the masses of the KK eigenstates associated to the Z boson.

We display in Fig. 2 the first four KK Z mass eigenvalues as a function of the KK photon mass, m_{KK}. As expected, m_{Z_1} and m_{Z_2} are almost degenerate and of the order m_{KK} (the first Z' mode mass is close to m_{KK}), with a mass splitting of $\sim$100−200 GeV, i.e., of the order of the electroweak scale (order of the off-diagonal mixing mass term). In the limit of zero mixing, Z_1 (Z_2) would correspond to the first KK mode of the Z' (Z) gauge boson. For similar reasons, m_{Z_3} and m_{Z_4} are nearly degenerate at a scale such that $m_{Z_3} - m_{Z_1}$ is much larger than the electroweak scale.

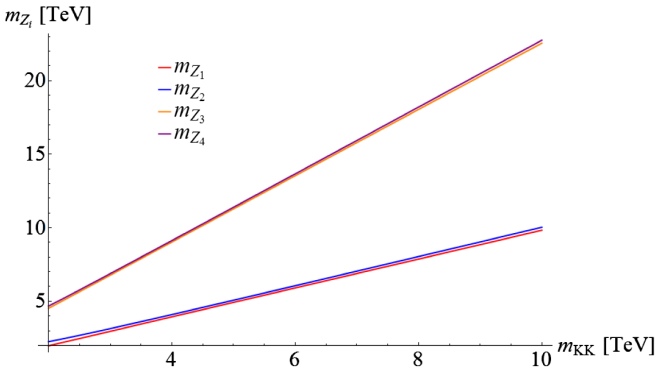

FIG. 2. Masses (in TeV) of the first four KK Z boson eigenstates, as a function of the first KK photon mass, m_{KK} (in TeV).

In fact, $\bar{m}_Z$ quantifies nothing else than the Higgs doublet VEV shift [23]. This phenomenon arises from the fact that the Z boson does not acquire its mass only from the scalar VEV, but also from mixing with the heavier KK partners. Therefore, to reproduce the very precisely measured m_Z, the VEV should be adjusted. To first nontrivial order in m_Z/m_{KK}, the RS VEV v gets shifted from its SM value $v_{\rm SM}$ as

$$v \simeq v_{\rm SM}\left(1+\frac{1+\alpha_Z^2}{2}\frac{3m_Z^2 kL}{m_{KK}^2}\right). \tag{15}$$

There are also other contributions at order m_Z^2/m_{KK}^2, but we do not display them, as they are not enhanced by the so-called volume factor, kL. Nevertheless, in our calculations we use the exact value of the obtained shifted VEV, v. As Eq. (15) already shows, the shifted VEV is always larger the SM VEV, i.e., $v > v_{\rm SM} = 246$ GeV (in the decoupling limit $m_{KK} \to \infty$, the two VEVs become equal, as expected).

For later use in the expression of the ϕZ and hZ cross sections, we also give the couplings of the Z_i eigenstates to the light fermions, which constitute the initial state for the process we are considering ($e^\pm$ for the ILC and light quark flavours, u, d, s, c, for the LHC). Since we consider the main intermediate states exchanged in the s channel, that is only the first $Z_{i=0,1,2}$ states, i.e., the Z boson and its first two excitations, we consider only their couplings to the light fermions. Such couplings can be inferred from the covariant derivative of the four-dimensional part of the kinetic term of the five-dimensional fermionic field,

$$S_\Psi^{\rm 5D} = \int {\rm d}^5x\sqrt{g}\bar{\Psi}i\Gamma^\mu D_\mu\Psi \to \int {\rm d}^5x\sqrt{g}\sqrt{L}\bar{\Psi}\Gamma^\mu \times (g_Z Q_Z^\Psi Z_\mu + g_{Z'}Q_{Z'}^\Psi Z'_\mu)\Psi, \tag{16}$$

where Ψ denotes a generic five-dimensional fermion, whose zero mode is a light SM fermion. The $\sqrt{L}$ factor allows us to use the four-dimensional couplings g_Z (defined in the previous subsections) and $g_{Z'} = g_R/\sqrt{g_R^2 - g_L^2\tan^2\theta_W}$, instead of their (dimensionful) five-dimensional equivalents. Meanwhile, $Q_{Z^{(\prime)}}^\Psi$ is the $Z^{(\prime)}$ charge of the fermion Ψ, given by

$$Q_Z^\Psi = I_{3L}^\Psi - Q_\gamma^\Psi \sin^2\theta_W, \qquad Q_{Z'}^\Psi = I_{3R}^\Psi - Y^\Psi\frac{g_L^2\tan^2\theta_W}{g_R^2}, \tag{17}$$

with $I_{3L/R}^\Psi$, Q_γ^Ψ, Y^Ψ being, respectively, the left/right isospin quantum number, electric charge, and hypercharge of the fermion Ψ. Denoting by $\exp(3ky/2)f(y)$ the profile of the light SM fermion originating from Ψ, one obtains its couplings to the Z_i bosons by plugging the KK decomposition in Eq. (8) into Eq. (16), thus obtaining

$$g_Z Q_Z^\Psi \int_0^L \frac{{\rm d}y}{L} f^2(y) g_+^i(y) + g_{Z'}Q_{Z'}^\Psi \int_0^L \frac{{\rm d}y}{L} f^2(y) g_-^i(y) \equiv g_Z Q_Z^\Psi c_i. \tag{18}$$

These couplings can easily be deduced from profile overlap considerations. First, note that the light fermion profiles, which are relevant for the initial state particles, are peaked towards the UV brane, with very small values close to the IR brane. Meanwhile, as shown in Fig. 1, the $g_\pm^{i=0,1,2}$ profiles are almost constant along the extra dimension, the sole exception being a small region near the IR brane, where they get peaked. Consequently, the overlap between the $g_\pm$'s and the light fermion profiles will effectively take place only in a region close to the UV brane, where the gauge boson profiles are almost constant. Therefore, bearing in mind that the fermion profiles are orthonormalized, the overlap between the light fermionic profiles and the gauge boson wave function is excellently approximated by the simple expression

$$c_i \simeq g_+^i(0)\int_0^L \frac{{\rm d}y}{L} f^2(y) = g_+^i(0). \tag{19}$$

The g_- profiles do not appear in this expression simply because their boundary conditions imply $g_-^i(0) = 0$. Therefore, in some sense, the light fermions couple only to the $\mathrm{SU}(2)_L \times \mathrm{U}(1)_Y$ part of the Z KK tower, which means that only their (SM-like) representations under the aforementioned gauge group are relevant for their coupling to the $Z_{0,1,2}$ states.

C. Higgs and radion couplings before mixing

We now focus on the radion and how it couples to the Z boson KK tower. We start by taking the background RS metric from Eq. (1) and including the scalar perturbation $F(x,y)$ as in Ref. [27],

$${\rm d}s^2 = {\rm e}^{-2(ky+F)}\eta_{\mu\nu}{\rm d}x^\mu{\rm d}x^\nu - (1+2F)^2{\rm d}y^2 \equiv \bar{g}_{MN}{\rm d}x^M{\rm d}x^N, \tag{20}$$

where we used $\bar{g}_{MN}$ to denote the five-dimensional metric with scalar perturbations included, in order to differentiate it from its unperturbed counterpart, g_{MN}. The linearized metric perturbations read

$$\bar{g}_{MN} - g_{MN} \equiv \delta g_{MN} \simeq -2F\,{\rm diag}({\rm e}^{-2ky}\eta_{\mu\nu}, 2). \tag{21}$$

The situation is slightly different for terms localized on the IR brane, i.e., terms that contain the Higgs bidoublet. On this brane, the line element is written as

$${\rm d}s_{\rm IR}^2 = {\rm e}^{-2[kL+F(x,L)]}\eta_{\mu\nu}{\rm d}x^\mu{\rm d}x^\nu \to {\rm e}^{-2F(x,L)}\eta_{\mu\nu}{\rm d}x^\mu{\rm d}x^\nu \equiv \bar{\eta}_{\mu\nu}{\rm d}x^\mu{\rm d}x^\nu, \tag{22}$$

where the arrow was used to indicate that the redefinition of the Higgs bidoublet H absorbs away the e^{-2kL} factor. Therefore, the linearized metric perturbations on the IR brane are given by

$$\bar{\eta}_{\mu\nu} - \eta_{\mu\nu} \equiv \delta\eta_{\mu\nu} \simeq -2F(x,L)\eta_{\mu\nu}. \tag{23}$$

In the limit of small backreaction (of the field F on the metric curvature), the scalar perturbation $F(x,y)$ can be parametrized as follows [27],

$$F(x,y) = \frac{\phi_0(x)}{\Lambda} e^{2k(y-L)}, \tag{24}$$

where ϕ_0 is the (unmixed) four-dimensional radion field[9] and Λ is the radion VEV, which is a $\mathcal{O}$ (TeV) energy scale that sets the length of the extra dimension [14]. At linear order, the radion's interaction with the gauge fields and the Higgs boson can be obtained by making the following replacements,

(i) $g^{MN} \to \bar{g}^{MN}$ in Eq. (2) for interactions originating from the bulk terms,
(ii) $d^4x \to d^4x\sqrt{\bar{\eta}}$, $\eta^{\mu\nu} \to \bar{\eta}^{\mu\nu}$ in Eq. (6) for brane-localized interactions,

and then keeping only the terms linear in F.[10] Finally, to derive the effective four-dimensional couplings, and take into account the KK Z mixings, one should employ the KK expansion from Eq. (8) and perform the usual integration over y (or, for the brane-localized terms, just evaluate the profiles in $y = L$). Thus, putting all these elements together, we arrive at the complete four-dimensional Lagrangian describing the h_0ZZ and ϕ_0ZZ interactions,

$$\begin{aligned}\mathcal{L}^{4D}_{\varphi Z_i Z_j} = \bar{m}_Z^2\left(\frac{h_0}{v} - \frac{\phi_0}{\Lambda}\right) C_i^{4D} C_j^{4D} Z_{i,\mu} Z_j^{\mu} \\ - \frac{\phi_0}{\Lambda}\left[\frac{m_{KK}^2}{3(kL)^2} C_{ij}^{5D} Z_{i,\mu} Z_j^{\mu} \right. \\ \left. + \frac{1}{2}\tilde{C}_{ij}^{5D} Z_{i,\mu\nu} Z_j^{\mu\nu}\right],\end{aligned} \tag{25}$$

where we have used the following notations:

$$C_i^{4D} = g_+^i(L) - \alpha_Z g_-^i(L), \tag{26}$$

$$C_{ij}^{5D} = L\int_0^L dy[(g_+^i)'(g_+^j)' + (g_-^i)'(g_-^j)'], \tag{27}$$

$$\tilde{C}_{ij}^{5D} = \frac{1}{L}\int_0^L dy e^{2k(y-L)}(g_+^i g_+^j + g_-^i g_-^j). \tag{28}$$

Let us now trace the origin of each term appearing in Eq. (25). The first term, proportional to $\bar{m}_Z^2$, originates from the brane-localized mass term in the first line of Eq. (6), whereas the terms between square brackets come from the five-dimensional gauge kinetic terms in Eq. (2). More precisely, in terms of five-dimensional fields, the first term between the square brackets originates from the $Z_{5\mu}Z^{5\mu}$ term, while the second one stems from $Z_{\mu\nu}Z^{\mu\nu}$.

We now have all the ingredients to derive the mixed Higgs-radion couplings to the Z_i bosons, which we do in the next section.

D. Higgs-radion mixing and couplings

The Higgs-radion mixing arises at the renormalizable level by coupling the four-dimensional Ricci scalar R_4 to the trace of $H^\dagger H$ via a possible gauge invariant term [26] as follows,

$$S_\xi^{4D} = \xi\int d^4x\sqrt{\bar{\eta}}R_4(\bar{\eta}_{\mu\nu})\frac{1}{2}\mathrm{tr}(H^\dagger H), \tag{29}$$

with $\bar{\eta}_{\mu\nu}$, the perturbed IR brane metric, defined in Eq. (22). As it involves the brane-localized Higgs field, the Higgs-radion mixing comes from the IR brane. A nonzero ξ coupling in Eq. (29) induces a kinetic mixing between the two scalars after EW symmetry breaking, the Higgs-radion Lagrangian at the quadratic level being given by [18,26,27]

$$\begin{aligned}\mathcal{L}^{4D}_{\varphi\varphi} = -\frac{1}{2}\begin{pmatrix}\phi_0 & h_0\end{pmatrix}\begin{pmatrix}1+6\xi\ell^2 & -3\xi\ell \\ -3\xi\ell & 1\end{pmatrix} \\ \times\begin{pmatrix}\Box\phi_0 \\ \Box h_0\end{pmatrix} - \frac{1}{2}m_{\phi_0}^2\phi_0^2 - \frac{1}{2}m_{h_0}^2 h_0^2,\end{aligned} \tag{30}$$

where $\ell \equiv v/\Lambda$ is the ratio between the Higgs and radion VEVs and $\Box$ is the flat-space d'Alembertian. The transition to the mass eigenstates, ϕ and h, is achieved through a nonunitary transformation diagonalizing the kinetic terms of Eq. (30),

$$\begin{pmatrix}\phi_0 \\ h_0\end{pmatrix} = \begin{pmatrix}a & -b \\ c & d\end{pmatrix}\begin{pmatrix}\phi \\ h\end{pmatrix}. \tag{31}$$

Using notations similar to the ones in Ref. [27], the elements of this matrix are $a = \cos\theta/Z$, $b = \sin\theta/Z$, $c = \sin\theta + t\cos\theta$, and $d = \cos\theta - t\sin\theta$, with $t = 6\xi\ell/Z$ and $Z^2 = 1 + 6\xi\ell^2(1-\xi)$ being the determinant of the kinetic mixing matrix from Eq. (30). The mixing angle is given by

[9]The KK radion modes are absorbed into the (longitudinal) degrees of freedom of the massive KK gravitons.

[10]Equivalently, one can find the radion couplings by varying the action with respect to the metric and keeping only the linear metric perturbations [27].

$$\tan\theta = \frac{m_{h_0}^2 - m_h^2}{t m_{h_0}^2} = -\frac{t m_{h_0}^2}{m_{h_0}^2 - m_\phi^2}. \tag{32}$$

The squared mass $m_{h_0}^2$ can then be expressed in terms of the physical mass eigenvalues $m_{h,\phi}$ as follows [26],

$$m_{h_0}^2 = \frac{Z^2}{2}\left[m_h^2 + m_\phi^2 + \mathrm{sign}(m_h^2 - m_\phi^2) \times \sqrt{(m_h^2 - m_\phi^2)^2 - \frac{144\xi^2\ell^2 m_h^2 m_\phi^2}{Z^2}}\right], \tag{33}$$

while $m_{\phi_0}^2$ can be deduced from $m_{h_0}^2 m_{\phi_0}^2 = Z^2 m_h^2 m_\phi^2$, which results from evaluating the mass matrix determinant in both bases. As it is clear from the expression of $m_{h_0}^2$ above, we use the sign convention in which m_h (m_ϕ) coincides with m_{h_0} (m_{ϕ_0}) when $\xi = 0$.

Summing up, the Higgs-radion system is described by four parameters: the mixing parameter ξ, the radion VEV Λ, the physical radion mass m_ϕ, and the physical Higgs mass m_h, which we fix at 125 GeV. There is also a fifth parameter, the first KK photon mass m_{KK}, which enters indirectly into this interplay by shifting the Higgs VEV. However, one cannot take arbitrary values for these parameters, as there are two theoretical consistency conditions that constrain the parameter space. The first condition is the absence of ghost fields in the theory, which restricts the kinetic mixing matrix determinant to positive values, i.e., $Z^2 > 0$. The second one concerns the square root appearing in Eq. (33), whose argument should be positive. This gives the following mathematical condition,

$$Z^2(m_h^2 - m_\phi^2)^2 \geq 144\xi^2\ell^2 m_h^2 m_\phi^2, \tag{34}$$

which actually supersedes the no-ghost condition, $Z^2 > 0$, in the whole parameter space. Note that, in the case of exact degeneracy between the Higgs boson and the radion, there can be no Higgs-radion mixing, as the condition in Eq. (34) imposes $\xi = 0$ if $m_h = m_\phi$.

We can now express the couplings of the physical Higgs and radion states to the gauge bosons. To ease the notations, we use the following definitions, which are similar to the ones in Ref. [27]:

$$g_\phi = c - \ell a, \qquad g_h = d + \ell b,$$
$$g_\phi^r = -\ell a, \qquad g_h^r = \ell b. \tag{35}$$

Using these definitions and the couplings of ϕ_0, h_0, which were derived in the previous section, one can straightforwardly write down the couplings for the scalar mass eigenstates, ϕ and h. As we are focusing on the $Z\phi$ (and Zh) production mechanism, we first list the Lagrangian for $\phi Z_i Z_j$ interactions, which is obtained by inserting the definitions of Eq. (35) in Eq. (25),

$$\begin{aligned}\mathcal{L}^{\mathrm{4D}}_{\phi Z_i Z_j} &= \frac{\bar{m}_Z^2}{v}\left(g_\phi C_i^{\mathrm{4D}} C_j^{\mathrm{4D}} + \frac{g_\phi^r m_{KK}^2}{3\bar{m}_Z^2 (kL)^2} C_{ij}^{\mathrm{5D}}\right)\phi Z_{i,\mu} Z_j^\mu \\ &\quad + \frac{g_\phi^r}{2v}\tilde{C}_{ij}^{\mathrm{5D}}\phi Z_{i,\mu\nu} Z_j^{\mu\nu} \\ &\equiv \frac{\bar{m}_Z^2}{v}\phi\left[C_{ij}^\phi Z_{i,\mu} Z_j^\mu + \frac{\tilde{C}_{ij}^\phi}{2\bar{m}_Z^2} Z_{i,\mu\nu} Z_j^{\mu\nu}\right].\end{aligned} \tag{36}$$

The hZ_iZ_j interactions are obtained by simply substituting $\phi \to h$ in the above equation.

We plot in Fig. 3, as a function of ξ and m_ϕ, the four couplings defined in Eq. (35), namely, $g_{\phi,h}$ and $g_{\phi,h}^r$. We have chosen $\Lambda = 4$ TeV, and, for simplicity, $m_{KK} \to \infty$. In fact, a finite m_{KK} would produce a shift in v and, as the four couplings depend on Λ only through the combination $\ell = v/\Lambda$, such a VEV shift can be compensated by adjusting Λ to give the same ℓ. Hence, the value of m_{KK} is not crucial in this context, which is why we have set it to infinity. As the four plots indicate, in most of the parameter space $g_{\phi,h}$ dominates over the $g_{\phi,h}^r$ coupling values. In practice, at currently accessible collider energies, one can ignore the $g_{\phi,h}^r$ couplings when calculating the $Z\phi$ or Zh production cross section (even if those coupling contributions are included in our numerical calculations). An exception to this rule applies in the vicinity of the $g_\phi = 0$ contour[11]: in this region, g_ϕ^r becomes dominant, and the radion's coupling to a pair of Z bosons is dramatically reduced, as is the $Z\phi$ production cross section, which tends to render this region blind to current hadronic or even future leptonic colliders. To conclude on this figure, in the limit of KK decoupling (where $C_0^{\mathrm{4D}} \to 1$), the radion coupling to two Z bosons corresponds mainly to g_ϕ [dimensionless with the normalization of Eq. (36)] and is thus driven by the Higgs-radion mixing [see Eq. (35)].

Before closing this section, let us remark on the correlation between the first KK photon/gluon mass, m_{KK}, and the radion VEV, Λ. The two quantities are related in the following way,

$$\frac{m_{KK}}{\Lambda} \simeq \frac{k}{M_{\mathrm{Pl}}}, \tag{37}$$

M_{Pl} being the Planck mass. In order to avoid significant five-dimensional quantum gravitational corrections, the above ratio should satisfy $k/M_{\mathrm{Pl}} \lesssim 3$ [34]. Throughout the paper we indeed systematically consider m_{KK} to be smaller than 3Λ. Even when the $m_{KK} \to \infty$ limit is considered, it means in fact that the KK partners are sufficiently heavy so as to not influence the numerical results, i.e., $m_{KK} = \mathcal{O}(10)$ TeV. Such values of m_{KK} do not conflict with the considered values of $\Lambda = 4$, 5 TeV.

[11]At high enough m_ϕ, the $g_\phi = 0$ condition becomes equivalent to the so-called conformal limit, $\xi = 1/6$.

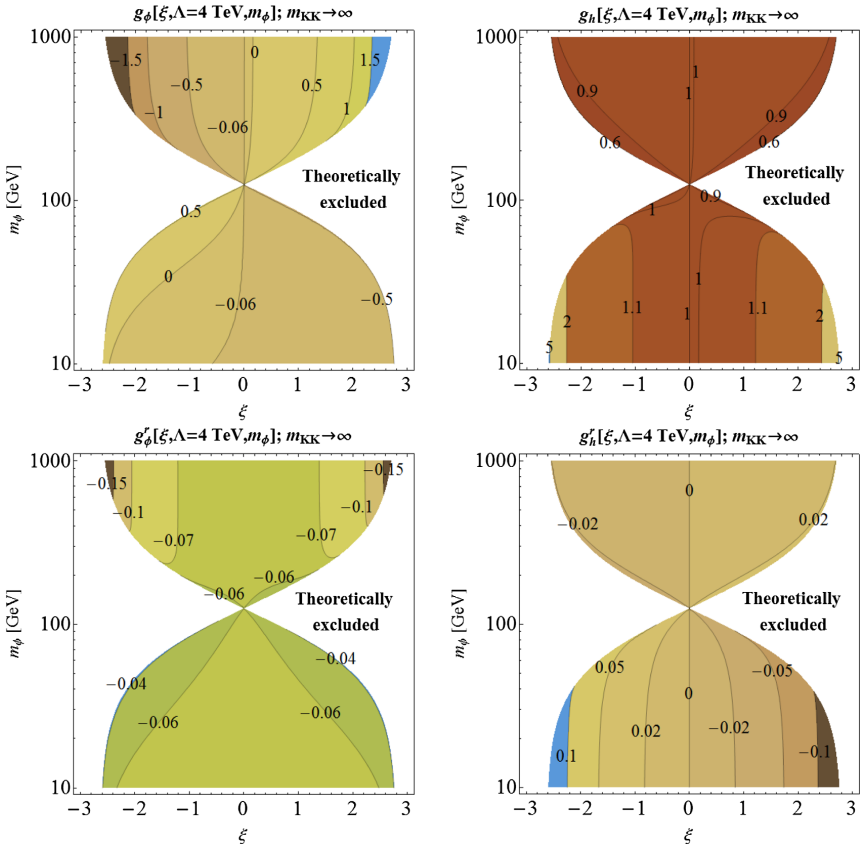

FIG. 3. Isocontours of the couplings (upper left) g_ϕ, (upper right) g_h, (lower left) g^r_ϕ, and (lower right) g^r_h, in the $\{\xi, m_\phi\}$ plane. The four dimensionless couplings plotted above are defined in Eq. (35). The white region is excluded by the theoretical consistency condition displayed in Eq. (34). The radion VEV Λ has been fixed at 4 TeV, while we have taken, for simplicity, $m_{KK} \to \infty$.

III. THE ϕZ AND hZ PRODUCTION

We now turn to the study of the $\phi Z/hZ$ production at the LHC and at the ILC, which proceeds through the s-channel exchange of Z_i bosons, $q\bar{q}/e^+e^- \to Z_i \to Z_0\phi/Z_0 h$. As higher KK levels are to a very good approximation decoupled, we only consider the Z boson plus its first two KK excitations, i.e., $i = 0, 1, 2$, as intermediate s-channel states. Moreover, in the LHC case, we consider only the dominant first and second generation quarks as initial state partons. The Feynman rule for the $Z_i Z_0 \phi$ vertex can be straightforwardly deduced from the Lagrangian piece in Eq. (36). We display below the squared absolute value of the spin-averaged and polarization-summed Lorentz invariant amplitude,

$$\begin{aligned}\overline{|\mathcal{M}_{\phi Z}|^2} = &\frac{g_Z^4(v_f^2+a_f^2)}{8}\\ &\times\sum_{i,j=0}^{2}\frac{c_i c_j s^2}{(s-m_{Z_i}^2+\mathrm{i}m_{Z_i}\Gamma_{Z_j})(s-m_{Z_j}^2-\mathrm{i}m_{Z_j}\Gamma_{Z_j})}\\ &\times\left[\frac{\bar{m}_Z^2}{m_Z^2}(\lambda\sin^2\theta^*+4r_Z)(C_{ij}^\phi)^2+8\sqrt{\lambda+4r_Z}C_{ij}^\phi\tilde{C}_{ij}^\phi\right.\\ &\left.+\frac{s}{\bar{m}_Z^2}(\lambda(1+\cos^2\theta^*)+12r_Z)(\tilde{C}_{ij}^\phi)^2\right], \qquad (38)\end{aligned}$$

where the coupling factors c_i are defined in Eq. (19). The notations we used are as follows: v_f and a_f are, respectively, the vectorial and axial couplings of the initial state fermions to the Z boson (i.e., $v_f = I_{3L}^f/2 - Q_\gamma^f \sin^2\theta_W$ and $a_f = I_{3L}^f/2$, with I_{3L}^f being the weak isospin of the fermion f, and Q_γ^f its electric charge), $\sqrt{s}$ the e^+e^-/partonic center-of-mass energy, and θ^* the scattering angle in the center-of-mass frame. Moreover, $\lambda = (1 - r_\phi - r_Z)^2 - 4r_\phi r_Z$, with $r_A = m_A^2/s$, is the usual two-body phase space function. The wave function overlap integrals c_i were defined previously in Eq. (19). As before, the amplitude for the Zh production process is obtained trivially from Eq. (38) by changing $\phi \to h$. The expression of the $\phi Z/hZ$ production cross section (in the case of the LHC, at the partonic level) is obtained from the integration over $\cos\theta^*$ of the amplitude displayed in Eq. (38).

As it is customary, we denote by Γ_{Z_i} the widths of the observed Z boson ($i = 0$) and of its first two KK excitations ($i = 1, 2$). In our calculations, as the (partonic) center-of-mass energy is always above m_{Z_0}, we can safely neglect Γ_{Z_0}. Regarding $Z_{1,2}$, their widths are approximately equal to 10% of their masses. For example, if one takes $m_{KK} = 3$ TeV, we get

$$m_{Z_1} \simeq 2.96 \text{ TeV}, \Gamma_{Z_1} \simeq 270 \text{ GeV} \quad \text{and}$$
$$m_{Z_2} \simeq 3.15 \text{ TeV}, \Gamma_{Z_2} \simeq 300 \text{ GeV}, \tag{39}$$

where we have chosen the dimensionless bulk mass parameters of the top and bottom quarks to be $c_{Q_L} = 0.4$, $c_{t_R} = 0$, and $c_{b_R} = -0.57$, such that their measured masses are reproduced and the left and right Zbb couplings are close to their SM values. These are values of the c-parameters that we use in our analysis. On the other hand, in order to explain the anomaly on the bottom quark forward-backward asymmetry A_{FB}^b at LEP (and, to a lesser extent, the anomalous top quark asymmetry A_{FB}^t measured at Tevatron), a more suitable choice would be $c_{Q_L} = 0.51$, $c_{t_R} = -1.3$, and $c_{b_R} = 0.53$ [31,32]. In this case, the widths of the KK Z partners change, but not dramatically: $\Gamma_{Z_1} \simeq 350$ GeV and $\Gamma_{Z_2} \simeq 275$ GeV. In both cases mentioned above, the Higgs-radion parameters have been fixed as follows: $\xi = 1$, $\Lambda = 4$ TeV, and $m_\phi = 750$ GeV. However, the width dependence on these parameters is weak, as the decay to $Z\phi$ is always subdominant. Throughout most of the parameter space spanned by ξ, Λ, and m_ϕ, with the c-parameters chosen above, the dominant decay channel for Z_1 (Z_2) is to WW (Zh).

A. At the LHC

1. Radion production

The LHC cross section is obtained by convoluting the cross section for the hard scattering, $\sigma(q\bar{q} \to Z_i \to Z\phi)$, with the parton distribution functions (PDFs). In the following, we use the MSTW set of PDFs at next-to-next-to-leading order [35].

We first show in Fig. 4 the $Z\phi$ production cross section as a function of m_ϕ and m_{KK}, for a proton-proton center-of-mass energy of $\sqrt{s} = 13$ TeV, with $\xi = 1$ and $\Lambda = 4$ TeV. We consider m_{KK} values above ~2 TeV as allowed from the direct Zh searches at the LHC (potentially affected by KK Z mixings), since there is no specific reason to expect unknown effects in this tree-level production—as discussed in the introduction. The radion mass range was discussed as well in Sec. I.

For $m_{KK} \gtrsim 5$ TeV, we see in Fig. 4 that the KK partners of the Z boson no longer play a significant role in the $Z\phi$ production, thus effectively decoupling. This is due to the fact that, at partonic center-of-mass energies $\sqrt{\hat{s}}$ bigger than ~5 TeV, or equivalently $\hat{s}/s \equiv \tau \gtrsim (5/13)^2$, the quark-antiquark luminosity drops down to a negligible level that restricts the on-shell production of $Z_{1,2}$ states. On the contrary, for $m_{KK} \lesssim 5$ TeV, the Z_1 and Z_2 states play an important role, but only for a radion heavier than ~500 GeV. This is because, in order to produce a radion plus a Z boson, $\sqrt{\hat{s}}$ should surpass $m_\phi + m_Z$, which means that, for a 500 GeV radion, the virtual Z boson contribution to the $Z\phi$ production is cut off by the $\sqrt{\hat{s}}$ threshold and hence becomes comparable to the contribution of its KK partners, Z_1 and Z_2. However, as one goes to lower radion masses, the cross section dependence on m_{KK} becomes less and less important, as the exchanged virtual Z boson becomes less and less off shell and starts to dominate over the contributions coming from the exchanges of Z_1 and Z_2. Nevertheless, we observe a small dependence on m_{KK} for small radion masses as well: its origin lies in the dependence of the $\phi Z_0 Z_0$ coupling on m_{KK}, which is a result of the mixing of the SM-like Z boson with its KK partners.

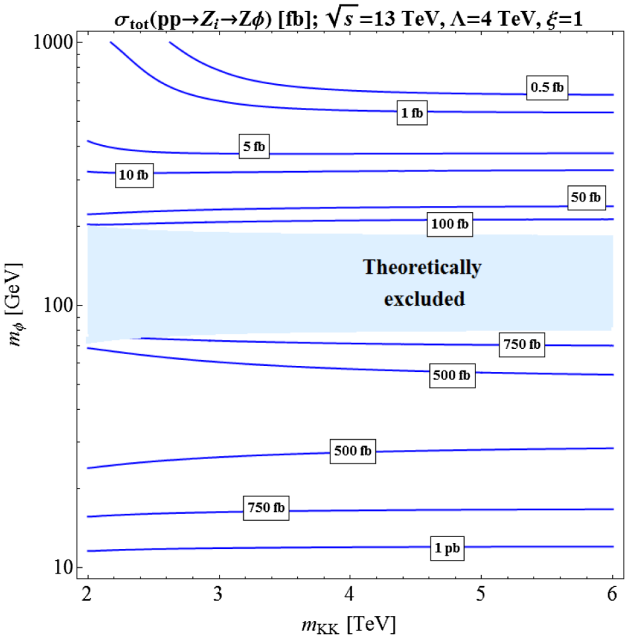

FIG. 4. Contour lines of the $Z\phi$ production cross section (in fb and pb) at the LHC in the plane m_ϕ (in GeV) versus m_{KK} (in TeV). The values of the other involved parameters are $\xi = 1$ and $\Lambda = 4$ TeV. The light blue region is excluded by the theoretical constraint from Eq. (34).

To better illustrate our argument from the previous paragraph, we show in Fig. 5 the $Z\phi$ invariant mass distribution for $\Lambda = 4$ TeV, $\xi = 1$, $m_{KK} = 3$ TeV, and two radion masses, $m_\phi = 10$ GeV (left panel) and $m_\phi = 750$ GeV (right panel). As the total cross section is obtained from the integration of the invariant mass distribution over values greater than the kinematical threshold, $\sqrt{\hat{s}} = m_{Z\phi} > m_\phi + m_Z$, it is clear why the KK Z partners play a role only for the associated production of a heavy radion: in this case, the integral does not cover the region at low $\hat{s}$, where the invariant mass distribution is enhanced by the reduced "off-shellness" of the Z boson contribution, thus giving more weight to the invariant mass region around the KK peak.

Moreover, one notices on the right panel of Fig. 5 that the two nearly degenerate KK Z bosons produce a single peak in the $Z\phi$ invariant mass distribution. In fact, as shown in this figure, this peak mostly originates from the Z_2 resonance, as it is, in general, more strongly coupled to

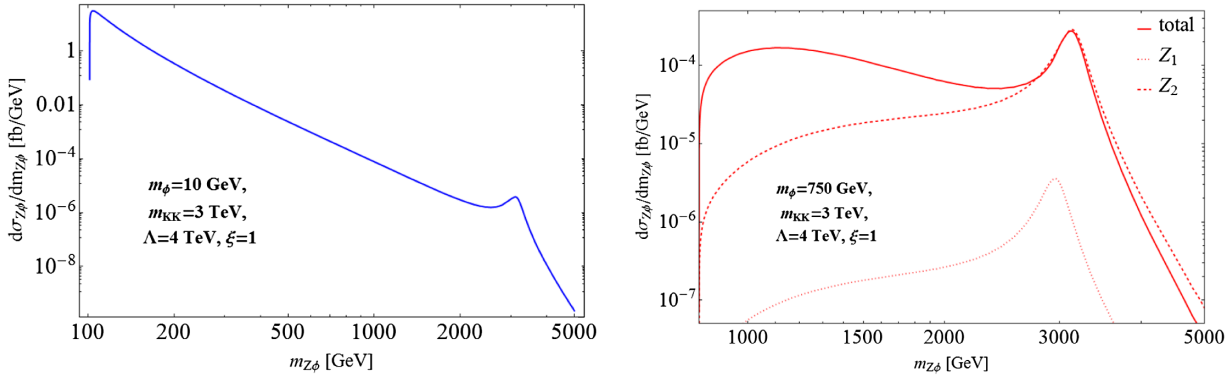

FIG. 5. $Z\phi$ invariant mass distribution at LHC (in fb/GeV) for (left) $m_\phi = 10$ GeV and (right) $m_\phi = 750$ GeV. The other parameters are fixed as follows: $m_{KK} = 3$ TeV, $\Lambda = 4$ TeV, and $\xi = 1$. On the right plot, we also display the individual contributions from the two KK boson eigenstates, Z_1 and Z_2.

$Z\phi$ than Z_1 is. The other reason is that the Z_1 eigenstate is mainly composed of the Z' boson, which has vanishing couplings to the light initial quarks localized towards the Planck brane. The interference term was taken at 0 to draw those two resonance distributions separately. The spectacular observation of such a resonant $Z\phi$ production would represent the simultaneous direct manifestation of the radion and the first KK Z boson, the rate of the extra boson Z' (mainly constituting the Z_1 state) resonance being probably too small to expect a detection at the LHC.

In addition, we have investigated the impact of varying the value of g_R on the $Z\phi$ production cross section at the LHC. For this, we have chosen a point in the plane displayed in Fig. 4 and computed the corresponding cross section for $g_R = g_L$ (left-right parity case [30]) and $g_R = 2g_L$ ($g_R \neq g_L$ is possible in different custodial symmetry implementations). Since one expects that changing g_R would affect mostly the KK Z bosons (not through small mixing effects, as is the case of Z_0), Z_1 and Z_2, we have considered $m_\phi = 800$ GeV, such that the heavy KK resonances have a sizeable contribution to the $Z\phi$ production. Furthermore, we have taken $m_{KK} = 3$ TeV and the other parameters as specified above the plot in Fig. 4. The $Z\phi$ production cross sections for the two values of g_R are of the same order of magnitude: while for $g_R = g_L$ we find ~0.5 fb, for $g_R = 2g_L$ the cross section value is ~0.15 fb. The difference comes mostly from the $Z_i Z_0 \phi$ ($i = 1, 2$) couplings, which are approximately two times stronger in the first case compared to the second case. The impact of the g_R variation on the cross section is independent of the ξ and Λ parameters.

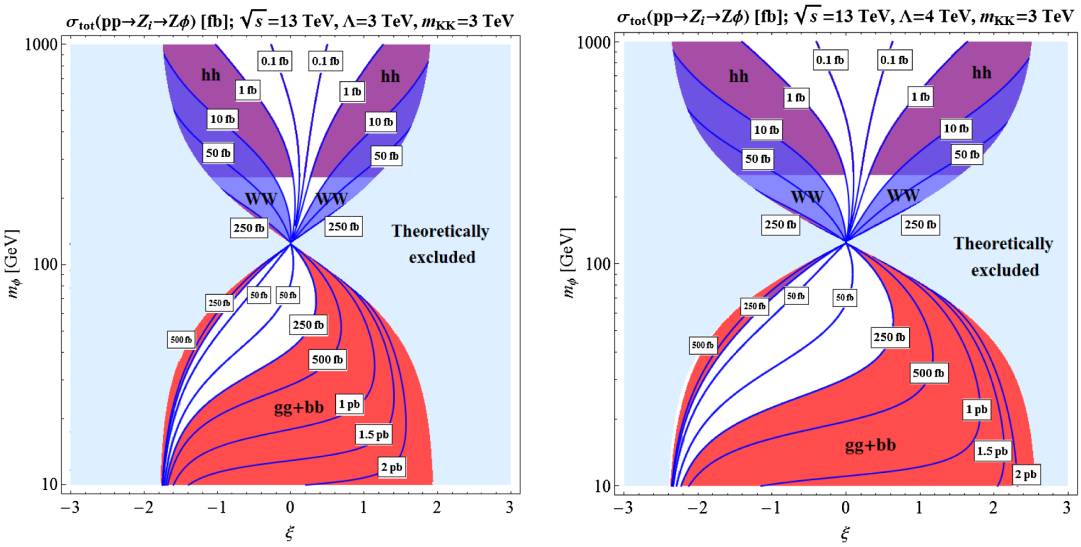

FIG. 6. Isocontours of $Z\phi$ production cross section (in fb and pb) at the LHC with $\sqrt{s} = 13$ TeV, as a function of ξ and m_ϕ (in GeV), for (left) $\Lambda = 3$ TeV and (right) $\Lambda = 4$ TeV with $m_{KK} = 3$ TeV. The light blue regions are excluded by the theoretical constraint from Eq. (34), while the purple, red, and blue zones approximately indicate parameter space regions that will be probed with 300 fb^{-1} at the LHC via radion decays into hh, dijets ($gg + bb$), and WW final states, respectively.

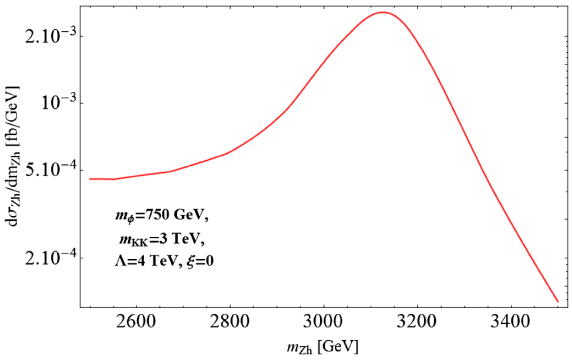

FIG. 7. Zh invariant mass distribution (in fb/GeV) in the neighborhood of the KK Z resonance peak, for $m_\phi = 750$ GeV. The values of the other relevant parameters are $m_{KK} = 3$ TeV, $\Lambda = 4$ TeV, and $\xi = 0$.

In Fig. 6, we present the total $Z\phi$ production cross section as a function of ξ and m_ϕ, for two values of the radion VEV, $\Lambda = 3, 4$ TeV, with m_{KK} fixed at 3 TeV in both cases. We observe that for $m_\phi > m_h$ the cross section contours have roughly the same behaviors as the g_ϕ ones (see Fig. 3). Indeed the dimensionless g_ϕ coupling corresponds in a good approximation to the radion coupling to two Z bosons as described in the comments of Fig. 3. This is no longer true for $m_\phi < m_h$: in this latter region, as explained in the previous paragraphs, the cross section typically increases as m_ϕ decreases, this being a result of the behavior of PDFs, which increase at lower values of $\tau = \hat{s}/s$. However, even for $m_\phi < m_h$, the lowest $Z\phi$ production cross sections are achieved in the vicinity of the $g_\phi = 0$ contour.

2. Higgs production

In Fig. 7, we show the Zh invariant mass distribution, focusing on the region close to the resonant peak produced by the almost degenerate Z_1 and Z_2 states (the peak, as in the case of $Z\phi$ production, originates mostly from Z_2). We have chosen the following realistic parameters: $m_\phi = 750$ GeV, $\Lambda = 4$ TeV, $\xi = 0$, and a mass of $m_{KK} = 3$ TeV. The Zh channel is a favored discovery avenue for Z_2, as the largest branching ratio of Z_2 is into Zh (meanwhile, Z_1 has its highest branching ratio for the WW decay). The observability potential for the KK resonance is discussed in Sec. IV A 4.

B. At the ILC

We now focus our attention on the $Z\phi$ production at a linear electron-positron collider, taking as an example the ILC. For an e^+e^- collider, the problem is simpler, as the center-of-mass energy is a known quantity and one does not need to convolute the cross section with PDFs.

Another simplifying aspect is the fact that, for ILC center-of-mass energies, which, in principle, could go up to 1 TeV, the s-channel exchange of the KK partners of the Z boson is negligible. Indeed as EWPT require that m_{KK} is larger than ~2–3 TeV, the two heavy resonances, Z_1 and Z_2, are significantly off shell even at $\sqrt{s} = 1$ TeV, which renders their contribution negligible. Therefore, effectively, only the Z boson exchange in the s channel has to be considered for the $Z\phi$ production, as we have numerically checked. Concerning

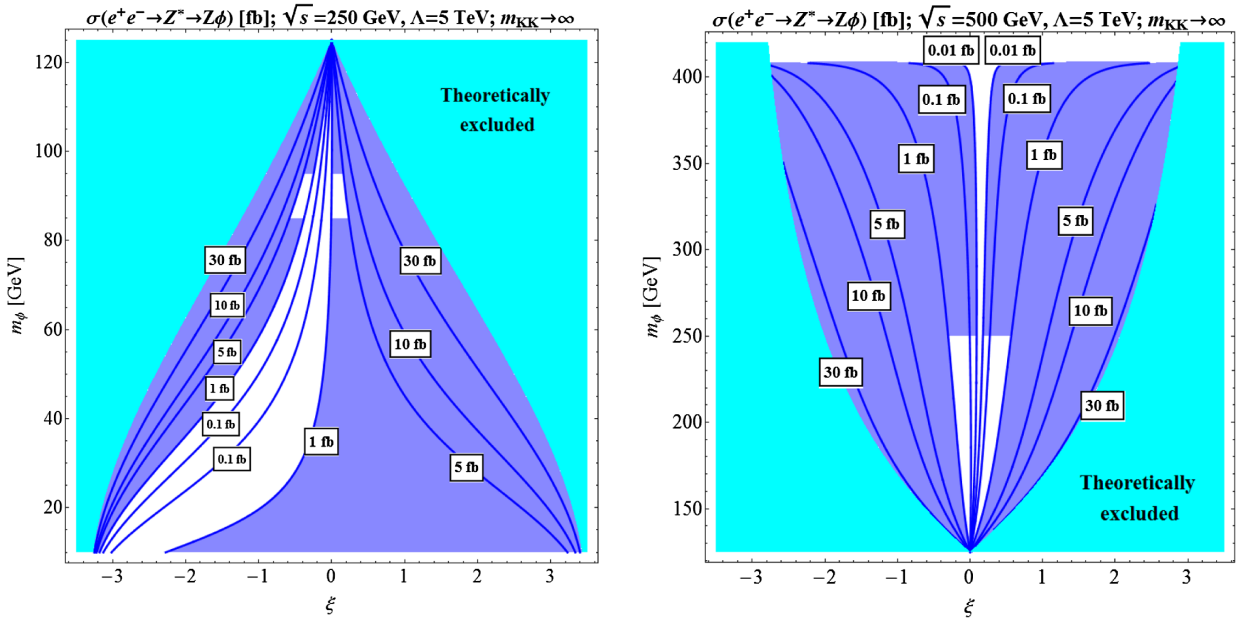

FIG. 8. Isocontours of the $Z\phi$ production cross section (in fb) at the ILC with (left) $\sqrt{s} = 250$ GeV or (right) $\sqrt{s} = 500$ GeV, in terms of ξ and m_ϕ (in GeV), for $\Lambda = 5$ TeV and $m_{KK} \to \infty$. The cyan regions are excluded by the theoretical constraint from Eq. (34), while the blue zones indicate the parameter space regions estimated to be probed at the ILC through the Z boson recoil mass technique.

the KK Z mixing effect on the ϕZZ coupling, for a given $Z\phi$ production cross section, varying m_{KK} translates to at most a percent-level shifting of ξ for a fixed m_ϕ.

We plot in Fig. 8 the $Z\phi$ production cross section in fb at the ILC, for e^+e^- center-of-mass energies of 250 and 500 GeV. We have chosen $\Lambda = 5$ TeV and, to ease the calculations, $m_{KK} \to \infty$ (see the previous paragraph). As described in Sec. III A 1, the hard process for the $Z\phi$ production cross section, as purely involved at the ILC (no PDF effects), has typically the same dependence on the two parameters ξ and m_ϕ, as the g_ϕ coupling itself, whose values are illustrated on Fig. 3 (as a matter of fact, to a very good approximation, the aforementioned cross section is proportional to g_ϕ^2). This explains the relative similarity of isocontour behaviors between Figs. 8 and 3 (upper left).

Notice that similarly to the SM Zh production, the $Z\phi$ cross section, for a given radion mass, is proportional to $1/s$.[12] Consequently, in order to present the regions with maximal rates, we show in Fig. 8 only small radion masses, $m_\phi < m_h$ for $\sqrt{s} = 250$ GeV, while, for $\sqrt{s} = 0.5$ TeV, we show only moderate to high radion masses, $m_\phi > m_h$.

IV. RADION, HIGGS, AND KK MODE DETECTION

A. At the LHC

1. Radion decay to $b\bar{b}$

For the full reaction $pp \to Z\phi$ followed by the radion decay into a bottom quark pair, $\phi \to b\bar{b}$ (possibly including the decay channel into two gluons), the SM background comes from double gluon radiation in the process $q\bar{q} \to Z$+2jets, which has been well studied at the LHC [36]. At a 13 TeV LHC energy, the full rate for the Z boson production followed by a muonic decay is $\sigma(pp \to Z)\, B(Z \to \mu^+\mu^-) \simeq 1900$ pb.

A drastic reduction of this background is therefore needed: it can come from a cut on the transverse momentum of the reconstructed Z, $p_T(\mu\mu) > 100$ GeV [see the $p_T(\mu\mu)$ distribution in Ref. [36]]. Such a cut would also induce a penalty on the $Z\phi$ production rate approximately equivalent to imposing a cut on the $Z\phi$ invariant mass distribution, $m_{Z\phi} > 200$ GeV, which would lead to a drastic reduction factor of $1/40$ for example for the distribution of Fig. 5 (left plot), obtained for a radion mass $m_\phi = 10$ GeV. For heavier radions, $m_\phi \gtrsim 100$ GeV, the effect of this optimal cut, $p_T(\mu\mu) > 100$ GeV, is not significant since the $Z\phi$ invariant mass distribution is defined on the range, $m_{Z\phi} > m_Z + m_\phi$. A softer cut, $p_T(\mu\mu) > 30$ GeV, would not alter significantly the signal, even for $m_\phi = 10$ GeV, and the background would be affected by a still efficient rejection factor of ∼20.

[12]Deviations from this behavior are proportional to g_ϕ^r, and in turn subdominant for most of the parameter space.

Let us now present guidelines on the main techniques to detect the $Z\phi$ production, depending on the radion mass.

$m_\phi \gtrsim 20$ GeV.—When $m_\phi \gtrsim 20$ GeV, it is justified to request two jets that further decrease by an order of magnitude the background (see Ref. [37] for an ATLAS analysis and Ref. [38] for a CMS one). Then a mass selection should gain a similar factor, which brings us to a rate of ∼1000 fb for the background. A bottom quark selection should gain an additional factor of 10–100 [39]. Therefore, assuming a future integrated luminosity of 300 fb^{-1} at the LHC, with a 20% reconstruction efficiency on the signal and background, this gives us a 250 fb sensitivity limit at 2σ on the cross section $\sigma_{\rm tot}(Z\phi)$, for a branching fraction $B(\phi \to b\bar{b}) \simeq 1$. This corresponds to selecting experimentally two inclusive jets (including two gluons or two b's). This LHC potential reach is illustrated in Fig. 6. On the obtained domains of the parameter space to which the LHC is potentially sensitive, one has indeed $B(\phi \to b\bar{b}) \simeq 1$, assuming standard radion branching ratios without unknown physics entering the radion-gluon-gluon triangular loop. With b tagging, the background should improve by about a factor 2 to 10 (corresponding to a factor up to $\sqrt{10}$ in the limit), depending on the tagging purity and efficiency, due to the further background reduction.

$m_\phi > 100$ GeV.—At higher masses, say $m_\phi > 100$ GeV, the $p_T(\mu\mu)$ selection cut can be increased up to 100 GeV without damaging the signal acceptance. Besides, for these masses, the mass resolution increases and therefore the sensitivity limit on $\sigma_{\rm tot}(Z\phi)$ should reach about 100 fb. This LHC potential reach covers higher mass regions in Fig. 6.

2. Radion decay to W^+W^-

$m_\phi > 160$ GeV.—In the regime $m_\phi > 160$ GeV, one benefits from the kinematical opening of the WW channel: $pp \to Z\phi$, $\phi \to W^+W^-$.[13] The radion branching ratio into ZZ is smaller. The associated SM background composed of the WWZ production has a cross section of ∼200 fb at 14 TeV including next-to-leading order QCD corrections [40]. Assuming an integrated luminosity of 300 fb^{-1} at the LHC and selecting semileptonic decays for the WW system for a reconstruction efficiency of 20% (not including leptonic branching ratios), one expects 170 events for this SM background. The radion mass selection then selects 20 events corresponding to a ∼20 fb sensitivity limit on the $\sigma_{\rm tot}(Z\phi)$ cross section, for a relevant branching $B(\phi \to W^+W^-) \simeq 0.5$, the associated sensitive region, for $m_\phi > 160$ GeV. This sensitivity order of magnitude is indicated in Fig. 6.

[13]One could benefit from a cut on the transverse momentum of the reconstructed Z as well based on such a $p_T(\mu\mu)$ distribution for the associated WWZ background.

3. Radion decay to hh

$m_\phi > 250$ GeV.—Finally, for $m_\phi > 250$ GeV, the LHC can become sensitive to the channel $pp \to Z\phi$, $\phi \to hh$. The Zhh production background opens up with a cross section of 0.25 fb [41]. Assuming a 20% reconstruction efficiency, including b tagging, would give a 0.5 event background. So three events from the $Z\phi$ signal would be sufficient for a 2σ detection. Hence one obtains a ∼5 fb cross section sensitivity limit for $\sigma_{\text{tot}}(Z\phi)$, with a realistic branching $B(\phi \to hh) \simeq 0.3$, the corresponding domain, for $m_\phi > 250$ GeV. The order of magnitude of this sensitivity is indicated in Fig. 6 as well.

This domain and the above sensitivity regions are clearly coarse estimates and a full analysis would be needed. Those regions however show that the $Z\phi$ search at the LHC could be complementary, in testing some specific regions of the $\{\xi, m_\phi\}$ plane, to the search for the gluon-gluon fusion mechanism of radion production, in case this loop-induced process is not affected by an unknown physics underlying the SM: this mechanism allows us to cover large domains of the RS parameter space as shown in the figures of Ref. [18] (regions below $m_\phi = 80$ GeV were not studied there).

4. KK resonances

The $Z\phi$ production can exhibit degenerate KK mode resonances made of Z boson excitations as described in Sec. IIIA. These resonances show up in the bump of Fig. 5. In order to discuss the possibility of a KK resonance observation in the radion production, we now consider some optimized but realistic parameter values, $\Lambda = 3$ TeV, $\xi = 1.5$, and $m_\phi = 500$ GeV (see the upper left plot of Fig. 3). Then the integrated rate of such a resonant process, obtained by considering an interval $m_{Z_2} \pm 2\Gamma_{Z_2}$ on Fig. 5, is of ∼10 fb (∼1 fb) for $m_{KK} = 2$ TeV (3 TeV). For a (HL-) LHC luminosity of 300(0) fb^{-1}, the induced number of events might lead to a possible but challenging observation. The kinematic selection of the interval around m_{KK} in the $Z\phi$ invariant mass distribution would reduce the associated SM background. The $p_T(\mu\mu)$ selection cut keeps a good efficiency if the production of $Z\phi$ is dominated by the exchange of a KK Z resonance. For $m_{KK} \simeq 2$ TeV and a radion mass below ∼120 GeV, a simple kinematical study shows that a cut $p_T(\mu\mu) \gtrsim 1$ TeV would select the signal peaked in this area while eliminating significantly the QCD background. A complete Monte Carlo simulation of the signal and background would be needed to conclude on the observability of such a resonance.

This $p_T(\mu\mu)$ selection method is generic and can even be applied for the various processes of the type $q\bar{q} \to Y \to XZ$ where Y is a heavy vector boson that can be produced on shell and X is a lighter resonance, either SM-like (W, Z, h) or exotic, as is the case for the radion. An additional advantage of this process is that it provides a combination of two resonances allowing a double discrimination. In this respect, the LHC could be competitive with the ILC where the production of an on-shell Y resonance is only possible for a mass $m_Y < 1$ TeV.

Similarly, the Zh production can occur through KK Z boson resonances as shown in Fig. 7. For the optimized parameter values, $\Lambda = 4$ TeV, $\xi = 1$, and $m_\phi = 500$ GeV (see the upper right plot of Fig. 3), and an optimistic low mass $m_{KK} \simeq 2$ TeV, the obtained integrated rate is of ∼11.5 fb. Similar remarks as for the $Z\phi$ production hold regarding the KK resonance observability.

5. Higgs production

The Higgs coupling to two Z bosons has been measured at the LHC, via the Higgs production in association with a Z boson. Assuming decoupling KK modes (which do not affect significantly the $Z\phi$ production), the Higgs couplings are modified only by the Higgs-radion mixing. Taking this into account, the experimental values for the hZZ coupling exclude some domains of the $\{\xi, m_\phi\}$ plane. However, as we see later on in Sec. IVB2, these domains are not significant when compared to the ILC sensitivity.

A first LHC analysis combines the run 1 measurements (ATLAS and CMS) [42], with global fits reporting a central value of ∼1 (i.e., SM value) and a ∼10% error at 1σ on g_h [defined in Eq. (35)[14] and denoted by κ_Z in Ref. [42]], assuming that the Higgs boson decays only into SM states. Therefore, in our case, this constraint is relevant only for $m_\phi > m_h/2$. Moreover, it allows for $0.6 < g_h^2 < 1.4$ at 2σ, which covers a tiny region in the g_h^2 plot from Fig. 9.

Reference [42] also presents global fits allowing for Higgs boson decays to non-SM states, but with the extra assumption that $g_h < 1$ (or $\kappa_Z < 1$ in their notation), which is not justified in our framework. Their result indicates that, at two sigma, $0.6 < g_h^2 < 1$, which means that, once again, only a tiny region from Fig. 9 is covered.

Even though, regarding the hZZ coupling measurement, the LHC is much less competitive than the ILC, these exclusions can still be seen as a new interpretation of the constraints on the RS model from the LHC Higgs data, in the presence of a Higgs-radion mixing (see also Ref. [43]). The Higgs physics appears naturally as complementary to the radion sector in testing their common $\{\xi, m_\phi\}$ parameter space.

B. At the ILC

1. Radion production

For the associated $Z\phi$ production at the ILC, one can use the same missing mass technique as for the Zh production [44], which is independent of the radion branching ratio

[14] In the $m_{KK} \to \infty$ limit employed here (where $C_0^{4D} \to 1$), g_h represents indeed the hZZ coupling normalized to its SM value, since the second term in Eq. (36) is vanishing in this limit and the third one is more than 2 orders of magnitude smaller.

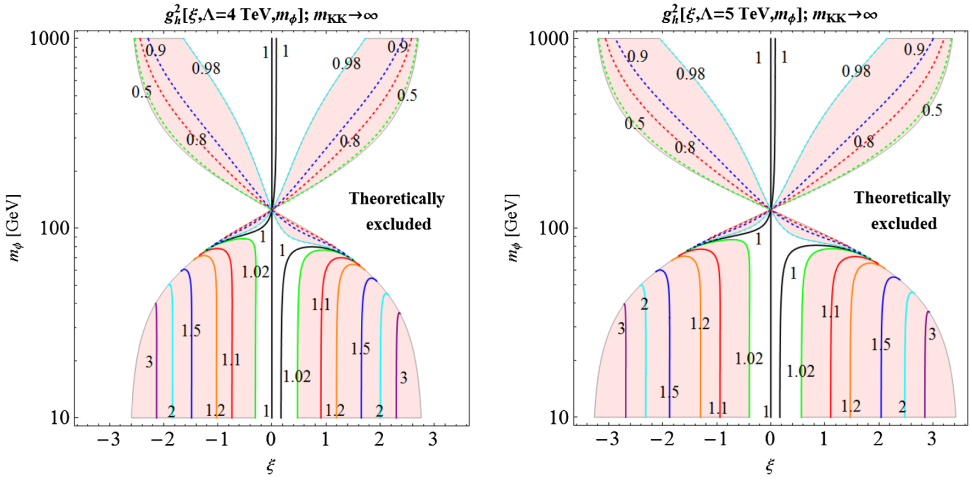

FIG. 9. Isocontours of g_h^2 in the $\{\xi, m_\phi\}$ plane, for (left) $\Lambda = 4$ TeV and (right) $\Lambda = 5$ TeV, with m_{KK} taken to infinity. The colored region indicates the future indirect sensitivity of the ILC on the Higgs-radion parameter space, corresponding to a ∼2% accuracy (at 2σ) on the measurement of the squared hZZ coupling, i.e., $0.98 < g_h^2 < 1.02$.

values. This powerful method is only feasible using the large luminosity provided by this machine, which plans to collect 2000 fb^{-1} at 250 GeV (H-20 scenario [45]), 4000 fb^{-1} at 500 GeV, and 8000 fb^{-1} at 1 TeV. This is to be compared to the LEP collider, which could only collect a few fb^{-1} per experiment so that LEP was not able to significantly exclude the presence of a radion at any mass. This recoil mass technique works best near the $Z\phi$ threshold where the center-of-mass energy is about $m_\phi + m_Z$. One then achieves the most precise recoil mass reconstruction. For this reason the low mass domain, $m_\phi \lesssim 160$ GeV, is covered by running at a center-of-mass energy of 250 GeV.

$m_\phi < m_Z$.—When $m_\phi < m_Z$, one has an easy situation. The Z background from ZZ^*/γ^* is distributed as a Breit Wigner with a small tail at low masses due to the virtual photon contribution from $Z\gamma^*$. The sensitivity reaches a limit on the $\sigma(Z\phi)$ of ∼1 fb at the 2σ statistical level. When the $b\bar{b}$ decay mode is considered, this sensitivity limit goes down even to 0.02 fb.

$m_\phi \sim m_Z$.—For $m_\phi \sim m_Z$, the ZZ background is the largest but still gives a sensitivity limit on $\sigma(Z\phi)$ of ∼3 fb at 2σ.

$m_\phi > m_Z$.—If $m_\phi > m_Z$, one ends up with a similar situation as for Zh: the main background comes from ZZ+ISR, where ISR stands for initial state radiation (i.e., a photon radiated off e^+/e^-), which, in most cases, remains undetected. The missing mass however includes both the Z and this photon, creating what one calls a radiative tail (for $m_\phi \sim m_Z$, the mass reconstruction of the Z into hadrons is too imprecise to allow a separation of m_ϕ from m_Z). From Ref. [44], one can easily evaluate the $\sigma(Z\phi)$ sensitivity in this mass region, which is at the 1 fb level. The Zh channel itself creates a background that generates a small blind zone for $m_\phi \simeq m_h$ but in this case the Higgs properties can also be altered allowing one to feel the presence of the radion.

$m_\phi > 130$ GeV.—At $m_\phi > 130$ GeV, it becomes possible to eliminate the radiative tail effect by reconstructing the radion mass through its decays into two jets. The $\sigma(Z\phi)$ sensitivity improves to 0.5 fb.

$m_\phi > 150$ GeV.—When $m_\phi > 150$ GeV, one starts crossing the kinematical limit for the $Z\phi$ production and it becomes necessary to use data taken at a 500 GeV center-of-mass energy. The recoil mass precision is poor since one operates far above the $Z\phi$ threshold, but the good energy resolution on jets ($\sigma E_j/E_j \sim 3\%$) allows us to use direct mass reconstruction with a mass resolution on the radion at the 2% level. One can then include the leptonic and neutrino decay modes from Z, gaining a factor ∼10 in efficiency. Since one is no longer suffering from the ISR effect this method turns out to give a sensitivity for $\sigma(Z\phi)$ at the 0.1 fb level.

$m_\phi > 160$ GeV.—For $m_\phi > 160$ GeV, the situation changes radically since the WW, ZZ channels become accessible for the radion decay, which helps the recoil techniques. For the SM background, Ref. [46] on WWZ cross sections shows that the WWZ contribution can be reduced down to 10 fb by using right-handed polarization (e_R) for the electron beam. The SM ZZZ background is at the 1 fb level. For ZWW one can simply use the $Z \to \mu\mu$ tagging. The WW component can be identified through semileptonic decays where a W decays hadronically and the other leptonically. Taking into account the branching ratios, one expects 350 background events. At the counting level one reaches a 1 fb sensitivity on $\sigma(Z\phi)$. One can then select the ϕ mass allowing an increased sensitivity of about 0.3 fb.

$m_\phi > 250$ GeV.—For $m_\phi > 250$ GeV, the hh channel becomes accessible for the radion decay. The Zhh SM background [47] is even smaller and with strong signatures given by the Higgs decay into $b\bar{b}$. Assuming a 50% efficiency with a relevant $B(\phi \to hh) \sim 0.3$ and low extra

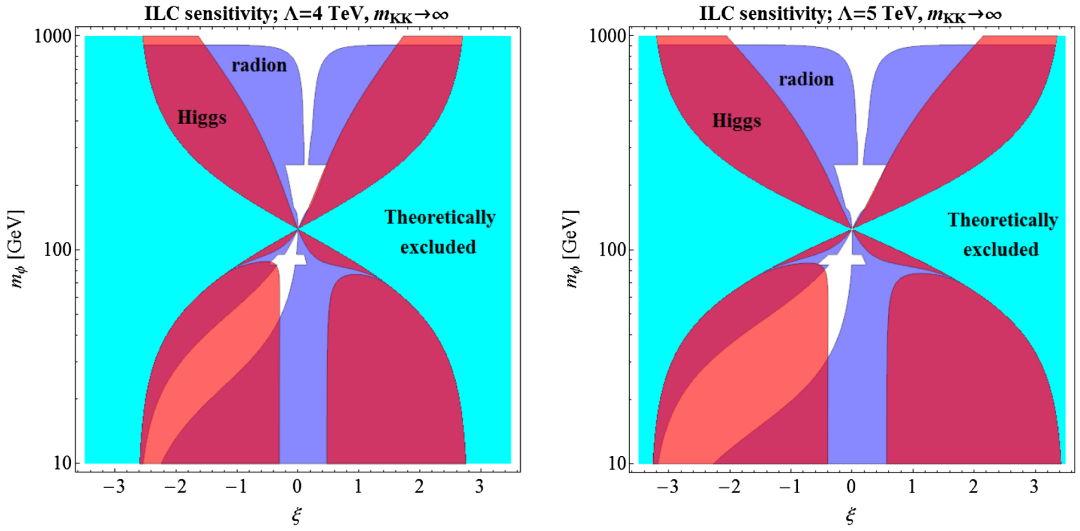

FIG. 10. Summary plots for direct and indirect radion searches at the three stages of operation of the ILC ($\sqrt{s} = 250$ GeV, 500 GeV, and 1 TeV), in the $\{\xi, m_\phi\}$ plane, for (left) $\Lambda = 4$ TeV and (right) $\Lambda = 5$ TeV, with m_{KK} taken to be infinite. The blue region covers the Higgs-radion parameter space estimated to be probed by the ILC through direct radion searches, while the red region represents the domain potentially probed by the precise measurement of the hZZ coupling. The theoretical constraint is superimposed once more, as the cyan domain.

backgrounds (from ZZZ essentially), one could reach a sensitivity on $\sigma(Z\phi)$ at the 0.01 fb level. For the other ILC option with a 1 TeV center-of-mass energy and an integrated luminosity of 8000 fb^{-1}, the factor increase in luminosity, compared to the 500 GeV scenario, induces a factor $\sqrt{2}$ of improvement in the cross section sensitivity (the Zhh background is only slightly smaller).

The various estimates given so far constitute a reasonable first guess of the ILC sensitivity for a radion search. All the obtained orders of magnitude for the sensitivities on $\sigma(Z\phi)$ given in the text are drawn as indicative colored regions in Fig. 8. In Fig. 10, we summarize in a unique plot the covered regions issued from two possible ILC runs respectively at 250 GeV, 500 GeV, and 1 TeV, for infinite m_{KK} (i.e., decoupled KK resonances) and two values of the radion VEV, $\Lambda = 4, 5$ TeV. A dedicated analysis is needed to fully assess such performances but it is clear that the ILC can dig into the radion scenario with excellent sensitivity.

We notice that the region corresponding to $\xi = 0$ and $m_\phi \simeq 60$–110 GeV, left uncovered in Fig. 10, might be tested via the search for the reaction $gg \to \phi \to \gamma\gamma$ at the HL-LHC extension with an integrated luminosity of 3000 fb^{-1}: this is the conclusion of Ref. [48] in the case of SM fields localized on the TeV brane.

Besides, as for the SM Higgs case, the vector boson fusion mechanism could provide additional information on the radion, in particular, allowing the determination of the total width and in turn of absolute widths [47].

2. Higgs production

The Higgs coupling to two Z bosons would possibly be measured at the 0.51% (1.3%) 1σ error level at the ILC with an energy option of 1 TeV (250 GeV), for a luminosity of 2500 fb^{-1} (250 fb^{-1}) [49], via the Higgs production in association with a Z boson. Such measurements would exclude at 2σ the regions of the $\{\xi, m_\phi\}$ plane, as illustrated in Fig. 9, assuming a central value equal to the predicted SM hZZ coupling constant. Notice that this measurement is independent of the Higgs branching ratio values due to the recoil technique used to tag the associated Z boson. The future precision Higgs physics at the ILC would thus be extremely efficient in testing the $\{\xi, m_\phi\}$ parameter space, as illustrated in Fig. 9. The obtained exclusion regions are superimposed as well on the summary plot of Fig. 10, showing the whole parameter space than can be covered using both the $Z\phi$ and Zh production at the ILC.

V. CONCLUSION

Let us finish this study on the radion production with a short conclusion, now that the numerical results have been discussed in detail with respect to the possibilities of observation. The investigation of the reaction $q\bar{q} \to Z\phi$ at the LHC could allow us to cover significant parts of the RS parameter space. This reaction could even benefit from the resonance of degenerate neutral KK vector bosons, which would enhance the reaction and allow for tight selections against the QCD background. It will take the ILC program at high luminosity to cover most of the theoretically allowed parameter space, via the $e^+e^- \to Z\phi$ search. The ILC, via such a reaction investigation, is particularly complementary of the LHC for testing the low radion masses (below the Higgs mass) since the reaction $gg \to \phi \to \gamma\gamma$ is quite efficient, in principle, to probe the high mass regime. The ILC benefits from the complementarity, of the direct radion searches and the high accuracy

measurements of the Higgs couplings, in the exploration of the RS parameter space (typically the $\{\xi, m_\phi\}$ plane).

ACKNOWLEDGMENTS

The authors gratefully acknowledge A. Ahmed, A. Djouadi, F. Nortier, and B. Rossignol for stimulating discussions. The work of A. A. is supported by the ERC advanced grant "Higgs@LHC." G. M. acknowledges the support from the CNRS Laboratoire International Associé (LIA), Theoretical High Energy Physics (THEP) and the Indo-French Network on High Energy Physics (INFRE-HEPNET) of the Indo-French Centre for the Promotion of Advanced Research (CEFIPRA/IFCPAR).

[1] L. Randall and R. Sundrum, Phys. Rev. Lett. **83**, 3370 (1999); M. Gogberashvili, Int. J. Mod. Phys. D **11**, 1635 (2002).
[2] R. Contino, Y. Nomura, and A. Pomarol, Nucl. Phys. **B671**, 148 (2003); K. Agashe, R. Contino, and A. Pomarol, Nucl. Phys. **B719**, 165 (2005); K. Agashe and R. Contino, Nucl. Phys. **B742**, 59 (2006); R. Contino, L. Da Rold, and A. Pomarol, Phys. Rev. D **75**, 055014 (2007).
[3] T. Gherghetta and A. Pomarol, Nucl. Phys. **B586**, 141 (2000); Y. Grossman and M. Neubert, Phys. Lett. B **474**, 361 (2000).
[4] For example, for quarks see G. Moreau, and J. I. Silva-Marcos, J. High Energy Phys. 03 (2006) 090; for charged leptons, G. Moreau and J. I. Silva-Marcos, J. High Energy Phys. 01 (2006) 048; and for neutrinos, G. Moreau, Eur. Phys. J. C **40**, 539 (2005).
[5] K. Agashe, A. Delgado, M. J. May, and R. Sundrum, J. High Energy Phys. 08 (2003) 050.
[6] C. Bouchart and G. Moreau, Nucl. Phys. **B810**, 66 (2009).
[7] R. Malm, M. Neubert, K. Novotny, and C. Schmell, J. High Energy Phys. 01 (2014) 173.
[8] S. Fichet and G. von Gersdorff, J. High Energy Phys. 03 (2014) 102.
[9] A. M. Iyer, K. Sridhar, and S. K. Vempati, Phys. Rev. D **93**, 075008 (2016); B. M. Dillon and S. J. Huber, J. High Energy Phys. 06 (2015) 066.
[10] P. R. Archer, M. Carena, A. Carmona, and M. Neubert, J. High Energy Phys. 01 (2015) 060.
[11] A. Falkowski and M. Perez-Victoria, J. High Energy Phys. 12 (2008) 107; J. A. Cabrer, G. von Gersdorff, and M. Quiros, Phys. Lett. B **697**, 208 (2011); J. High Energy Phys. 05 (2011) 083.
[12] R. Contino, L. Da Rold, and A. Pomarol, Phys. Rev. D **75**, 055014 (2007).
[13] C. Csaki, M. Graesser, L. Randall, and J. Terning, Phys. Rev. D **62**, 045015 (2000).
[14] W. D. Goldberger and M. B. Wise, Phys. Lett. B **475**, 275 (2000).
[15] C. Csaki, M. L. Graesser, and G. D. Kribs, Phys. Rev. D **63**, 065002 (2001).
[16] S. Gopalakrishna, T. Mandal, S. Mitra, and G. Moreau, J. High Energy Phys. 08 (2014) 079; R. Barceló, S. Mitra, and G. Moreau, Eur. Phys. J. C **75**, 527 (2015).
[17] B. Lillie, L. Randall, and L. T. Wang, J. High Energy Phys. 09 (2007) 074; B. Lillie, J. Shu, and T. M. P. Tait, Phys. Rev. D **76**, 115016 (2007); F. Ledroit, G. Moreau, and J. Morel, J. High Energy Phys. 09 (2007) 071; A. Djouadi, G. Moreau, and R. K. Singh, Nucl. Phys. **B797**, 1 (2008); M. Guchait, F. Mahmoudi, and K. Sridhar, Phys. Lett. B **666**, 347 (2008); K. Agashe, A. Belyaev, T. Krupovnickas, G. Perez, and J. Virzi, Phys. Rev. D **77**, 015003 (2008); B. C. Allanach, F. Mahmoudi, J. P. Skittrall, and K. Sridhar, J. High Energy Phys. 03 (2010) 014; A. Angelescu *et al.*, arXiv:1512.03047.
[18] M. Frank, K. Huitu, U. Maitra, and M. Patra, Phys. Rev. D **94**, 055016 (2016).
[19] ATLAS Collaboration, https://twiki.cern.ch/twiki/bin/view/AtlasPublic.
[20] CMS Collaboration, http://cms-results.web.cern.ch/cms-results/public-results/publications/.
[21] R. Malm, M. Neubert, and C. Schmell, J. High Energy Phys. 02 (2015) 008.
[22] A. Djouadi and G. Moreau, Phys. Lett. B **660**, 67 (2008).
[23] C. Bouchart and G. Moreau, Phys. Rev. D **80**, 095022 (2009).
[24] F. Richard, arXiv:1604.01640.
[25] K. Agashe, P. Du, S. Hong, and R. Sundrum, J. High Energy Phys. 01 (2017) 016.
[26] G. F. Giudice, R. Rattazzi, and J. D. Wells, Nucl. Phys. **B595**, 250 (2001); C. Csáki, M. L. Graesser, and G. D. Kribs, Phys. Rev. D **63**, 065002 (2001); D. Dominici, B. Grzadkowski, J. F. Gunion, and M. Toharia, Nucl. Phys. **B671**, 243 (2003).
[27] C. Csáki, J. Hubisz, and S. J. Lee, Phys. Rev. D **76**, 125015 (2007); A. Ahmed, B. M. Dillon, B. Grzadkowski, J. F. Gunion, and Y. Jiang, Phys. Rev. D **95**, 095019 (2017).
[28] P. Cox, A. D. Medina, T. S. Ray, and A. Spray, J. High Energy Phys. 02 (2014) 032.
[29] K. Agashe, H. Davoudiasl, S. Gopalakrishna, T. Han, G.-Y. Huang, G. Perez, Z.-G. Si, and A. Soni, Phys. Rev. D **76**, 115015 (2007).
[30] K. Agashe, R. Contino, L. Da Rold, and A. Pomarol, Phys. Lett. B **641**, 62 (2006).
[31] A. Djouadi, G. Moreau, and F. Richard, Nucl. Phys. **B773**, 43 (2007).
[32] A. Djouadi, G. Moreau, F. Richard, and R. K. Singh, Phys. Rev. D **82**, 071702 (2010); A. Djouadi, G. Moreau, and F. Richard, Phys. Lett. B **701**, 458 (2011).
[33] A. Azatov, M. Toharia, and L. Zhu, Phys. Rev. D **82**, 056004 (2010).

[34] K. Agashe, H. Davoudiasl, G. Perez, and A. Soni, Phys. Rev. D **76**, 036006 (2007).
[35] A. D. Martin, W. J. Stirling, R. S. Thorne, and G. Watt, Eur. Phys. J. C **63**, 189 (2009).
[36] The CMS Collaboration, Report No. CMS PAS SMP-15-011.
[37] The ATLAS Collaboration, Report No. ATLAS-CONF-2016-046.
[38] The CMS Collaboration, Report No. CMS-SMP-14-005.
[39] The ATLAS Collaboration, J. High Energy Phys. 10 (2014) 141.
[40] D. T. Nhung, L. D. Ninh, and M. M. Weber, J. High Energy Phys. 12 (2013) 096.
[41] Q.-H. Cao, Y. Liu, and B. Yan, Phys. Rev. D **95**, 073006 (2017).
[42] The ATLAS and CMS Collaborations, Report No. ATLAS-CONF-2015-044.
[43] A. Chakraborty *et al.*, arXiv:1701.07471.
[44] H. Li, R. Pöschl, and F. Richard, arXiv:1202.1439.
[45] T. Barklow *et al.*, Report No. ILC-NOTE-2015-068.
[46] P. Doublet, Ph.D. thesis, 2011, http://publication.lal.in2p3.fr/2011/These-PhDoublet.pdf.
[47] *The International Linear Collider Technical Design Report—Volume 2: Physics*, edited by H. Baer *et al.* (ILC Report No. ILC-REPORT-2013-040), p. 37.
[48] S. Bhattacharya, M. Frank, K. Huitu, U. Maitra, B. Mukhopadhyaya, and S. K. Rai, Phys. Rev. D **91**, 016008 (2015).
[49] J. Tian *et al.* (ILC physics and detector study Collaboration), Nucl. Part. Phys. Proc. **273–275**, 826 (2016).